# CORONAL PROPERTIES OF *Swift*/BAT-SELECTED SEYFERT 1 AGN OBSERVED WITH *NuSTAR*

N. KAMRAJ[1], F. A. HARRISON[1], M. BALOKOVIĆ[2], A. LOHFINK[3], M. BRIGHTMAN[1]

*Draft version September 7, 2018*

## ABSTRACT

The *NuSTAR* observatory, with its high sensitivity in hard X-rays, has enabled detailed broadband modeling of the X-ray spectra of Active Galactic Nuclei (AGN), thereby allowing constraints to be placed on the high-energy cutoff of the X-ray coronal continuum. We investigate the spectral properties of a sample of 46 *NuSTAR*-observed Seyfert 1 AGN selected from the *Swift*/BAT 70-month hard X-ray survey. Our measurements of the high-energy cutoff of the continuum from modeling the *NuSTAR* X-ray spectra are used to map out the temperature – compactness ($\theta - l$) plane for AGN coronae. We find that most of the coronae lie clustered near the boundary for runaway pair production, suggesting that annihilation and pair production act to regulate the temperature of the corona. We discuss the implications of coronae whose high-energy cutoff may indicate a low coronal temperature on the heating and thermalization mechanisms in the corona.

*Subject headings:* black hole physics: galaxies – galaxies: active – X-rays: galaxies

## 1. INTRODUCTION

The continuum X-ray emission from Active Galactic Nuclei (AGN) is believed to originate in a hot, compact corona located above the accretion disk (e.g., Haardt & Maraschi 1993). Compton upscattering of UV and optical photons from the inner accretion disk by coronal electrons produces a power-law-like X-ray continuum, with a cutoff at energies determined by the electron temperature $T_e$ (e.g., Rybicki & Lightman 1979; Zdziarski et al. 2000). The shape of the coronal continuum is sensitive to properties such as the seed photon field, electron temperature, optical depth, and observer viewing angle. The observed rapid variability of the 2–10 keV emission in many AGN, combined with X-ray spectral timing and reverberation mapping, strongly indicate that the corona is physically compact, of the order 3–10 gravitational radii (Fabian et al. 2009; Kara et al. 2013; Emmanoulopoulos et al. 2014; Fabian et al. 2015). The gravitational radius is defined to be $GM_{\rm BH}/c^2$, where $M_{\rm BH}$ is the supermassive black hole mass. Such radiatively compact sources can exchange significant energy between particles and photons, with the compactness characterised by the dimensionless parameter $l$ (Guilbert et al. 1983), defined as:

$$l = 4\pi \frac{m_p}{m_e} \frac{R_g}{R} \frac{L}{L_E} \qquad (1)$$

where $m_p$ and $m_e$ are the proton and electron mass respectively, $R_g$ is the gravitational radius, $R$ the source radius, $L$ the source luminosity, and $L_E$ the Eddington luminosity. The electron temperature $T_e$ can also be characterised by the dimensionless parameter $\theta = k_B T_e/m_e c^2$, where $k_B$ is the Boltzmann constant. For sufficiently energetic photons, photon-photon collisions

can lead to electron-positron pair production in the corona (Svensson 1982; Guilbert et al. 1983; Zdziarski 1985). At high coronal temperatures, when the Wien tail of the power-law spectrum extends above $2m_e c^2$, pair production can quickly become a runaway process, exceeding annihilation (Svensson 1984). This will limit any further rise in temperature, thus acting as an $l$-dependent thermostat (Svensson 1984; Zdziarski 1985; Stern et al. 1995).

The *NuSTAR* observatory (Harrison et al. 2013), being the first focusing hard X-ray telescope in orbit, has enabled detailed, high signal-to-noise spectra to be obtained in the 3–79 keV band for many local AGN. *NuSTAR* spectral modeling can thus place constraints on the spectral photon index and high-energy cutoff of the coronal X-ray continuum, enabling robust estimates of $l$ and $\theta$. One of the primary goals of the *NuSTAR* mission is to perform an extragalactic survey of the hard X-ray sky, in order to characterise the AGN population. We define hard X-rays as photons with energies > 10 keV. As part of its Extragalactic Legacy Surveys program[4], the *NuSTAR* observatory has performed snapshot ∼ 20 ks observations of local AGN detected in the all-sky survey with the Burst Alert Telescope (BAT) instrument onboard the *Neil Gehrels Swift Observatory* (Gehrels et al. 2004; Baumgartner et al. 2013). Though previous work has provided broad constraints on the high-energy cutoff for samples of bright AGN, tight constraints for particular AGN only became available recently thanks to *NuSTAR* (e.g., Ballantyne et al. 2014; Brenneman et al. 2014; Marinucci et al. 2014; Fabian et al. 2015; Baloković et al. 2015). The 100-fold increase in sensitivity of the *NuSTAR* telescope compared to the *Swift*/BAT instrument enables robust spectral modeling with a minimal *NuSTAR* exposure of ∼ 20 ks. With even longer exposure *NuSTAR* observations, it is possible to obtain tight limits on X-ray spectral parameters and perform reverberation mapping measurements of coronal size.

In this paper, we study a sample of 46 *Swift*/BAT se-

Contact: nkamraj@caltech.edu
[1] Cahill Center for Astronomy and Astrophysics, California Institute of Technology, Pasadena, CA 91125, USA
[2] Harvard-Smithsonian Center for Astrophysics, 60 Garden Street, Cambridge, MA 02138, USA
[3] Department of Physics, Montana State University, 211 Montana Hall, Bozeman, MT 59717, USA

[4] https://www.nustar.caltech.edu/page/legacy_surveys

arXiv:1809.01757v1 [astro-ph.HE] 5 Sep 2018

lected Seyfert 1 (Sy1) AGN observed with *NuSTAR*, in order to map out the location of these sources on the temperature – compactness ($\theta-l$) diagram for AGN coronae. We do not include *Swift*/XRT data in our spectral modeling as the limited data quality of available simultaneous *Swift*/XRT data introduces difficulties in obtaining constraints on parameters such as the cutoff energy. The complexity of features in soft X-ray spectra would ideally require high signal-to-noise ratio, simultaneous spectra from soft X-ray telescopes with larger collecting area to model robustly, which are currently unavailable for the targets in our sample. In section 2, we discuss the sample used in this study, the data reduction, and analysis procedures adopted. Observational details of our AGN sample are presented in Table 2 of the appendix. In section 3, we present our results and discuss the heating and cooling mechanisms operating in the corona. We discuss future, deeper *NuSTAR* observations of AGN in our sample with potential cutoffs in the *NuSTAR* band in section 4, and present a summary in section 5. In this work, all uncertainties were calculated at the 90% confidence level and standard values of the cosmological parameters ($h_0 = 0.7$, $\Omega_\Lambda = 0.7$, $\Omega_m = 0.3$) were used to calculate distances.

## 2. SAMPLE, DATA REDUCTION, AND ANALYSIS

### 2.1. *Sample of Seyfert 1 AGN*

We selected our sample from AGN identified in the *Swift*/BAT 70–month hard X-ray catalogue (Gehrels et al. 2004; Baumgartner et al. 2013). From the full catalogue, we selected *NuSTAR*-observed AGN with known redshifts and classified as Sy1 from optical hydrogen emission line measurements, or from available data from the NASA/IPAC Extragalactic Database (NED). The full list of AGN included in our study, along with their *NuSTAR* observation details, may be found in Table 2 of the appendix. Figure 1 shows the location of our sources on the redshift-luminosity plane, with the luminosity values determined from the *Swift*/BAT fluxes in the 14–195 keV range. We confirmed sources at high redshift to not be beamed AGN or blazar candidates from observations of their optical spectra and cross-matching with the Roma Blazar Catalog (Massaro et al. 2009). We found two sources which were misclassified from NED and were removed from our sample. We excluded 9 sources from our original sample due to lack of constraints on the high-energy cutoff from spectral fitting. Our final sample consists of 46 Sy1 AGN at $0.003 < z < 0.2$.

In Figure 2, we present the distributions of *Swift*/BAT fluxes, luminosities and redshifts for both our sample and the Sy1 classified sources from the *Swift*/BAT 70-month catalog. We find that our sample is statistically representative of the Sy1 population from the *Swift*/BAT 70-month catalog, with the mean and median values overlapping between our sample and the parent *Swift*/BAT sample. We further applied a two-sample Kolmogorov-Smirnov test and found the K-S test statistic to be 0.1 or lower, and the p-value above 60 % for all three distributions, thus confirming that the distributions are consistent between our sample and the larger *Swift*/BAT sample of Sy1s.

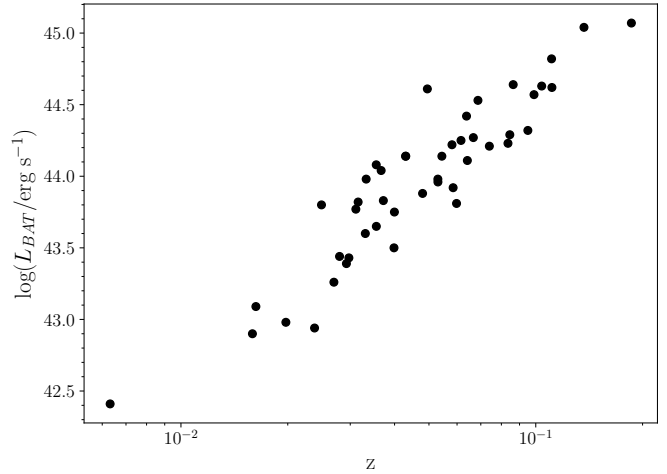### 2.2. *NuSTAR Observations and Data Reduction*



FIG. 1.— Redshift-luminosity distribution for *NuSTAR*-observed Sy1 AGN selected from the *Swift*/BAT 70-month hard X-ray catalogue.

Roughly once per week since its start of science operations in 2013, the *NuSTAR* satellite has been obtaining $\sim 20$ ks observations in the 3–79 keV band of AGN selected from the *Swift*/BAT 70-month hard X-ray catalog (Baumgartner et al. 2013). We performed reduction of raw event data from both *NuSTAR* modules, FPMA and FPMB (Harrison et al. 2013), using the *NuSTAR* Data Analysis Software (NuSTARDAS, version 1.2.1), distributed by the NASA High Energy Astrophysics Archive Research Center (HEASARC) within the HEASOFT package, version 6.16. We took instrumental responses from the *NuSTAR* calibration database (CALDB), version 20160502. Raw event data were cleaned and filtered for South Atlantic Anomaly (SAA) passages using the `nupipeline` module. We extracted source and background energy spectra from the calibrated and cleaned event files using the `nuproducts` module. Detailed information on these data reduction procedures can be found in the *NuSTAR* Data Analysis Software Guide (Perri et al. 2014). An extraction radius of $30''$ was used for both the source and background regions. We extracted the background spectrum from source-free regions of the image, and away from the outer edges of the field of view, which have systematically higher background. The spectral files were rebinned using the HEASOFT task `grppha` to give a minimum of 20 photon counts per bin. For multiple observations of the same source, we coadded spectra using the HEASOFT task `addspec`.

### 2.3. *Spectral Modeling*

We performed spectral modeling of the *NuSTAR* data in the 3–79 keV band for each source in our sample using XSPEC v12.8.2 (Arnaud 1996). We used $\chi^2$ statistics for all model fitting and error estimation. We adopted cross sections from Verner et al. (1996) and solar abundances from Wilms et al. (2000). In all our modeling we include a cross-correlation constant between FPMA and FPMB to account for slight differences in calibration (Madsen et al. 2015)

We fit each spectrum with an absorbed power-law model with a high-energy cutoff, $E_{cut}$. The slope of the power-law continuum is characterized by the pho-
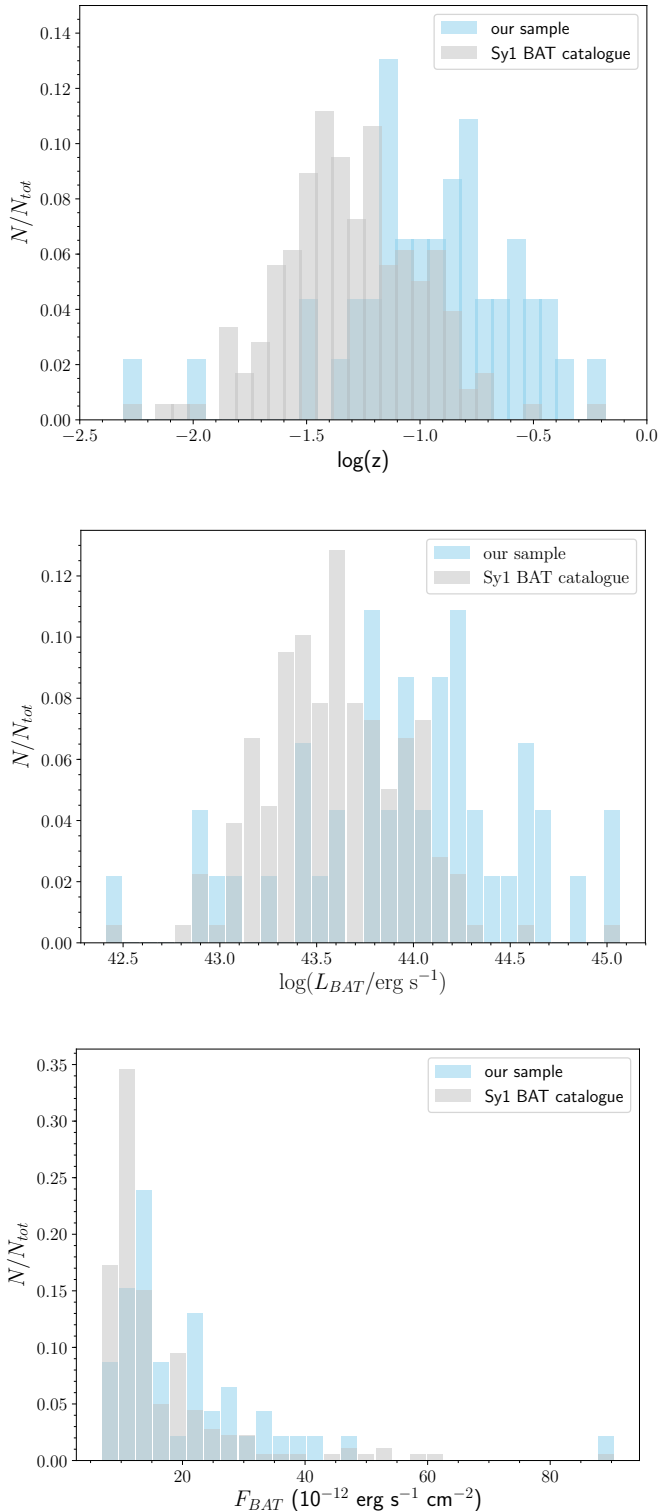
FIG. 2.— Distributions of redshifts, *Swift*/BAT 70-month X-ray catalogue luminosities and fluxes for both our sample and the Sy1 classified sources from the *Swift*/BAT catalogue. For clarity, sources with $L_{BAT} < 10^{40}$ erg s$^{-1}$ and $F_{BAT} > 1 \times 10^{-10}$ erg s$^{-1}$ cm$^{-2}$ were omitted from the plots.

ton index, $\Gamma$. It is assumed that the instrinsic continuum intensity is proportional to $E^{-\Gamma}\exp(-E/E_{\rm cut})$. In XSPEC notation, the model used is `TBabs` $\times$ `zwabs` $\times$ `cutoffpl`, where the component `TBabs` models Galactic absorption, which is fixed to a typical Galactic column density of $7.6 \times 10^{21}$ cm$^{-2}$ (Kalberla et al. 2005). We found that freezing the Galactic column density did not have any significant effect on the fit results, as spectral modeling over the hard X-ray band is relatively insensitive to this parameter. The redshifted component `zwabs` accounts for absorption by the host galaxy.

Where an Fe K$\alpha$ emission line feature was observed in the spectra at 6.4 keV, we added an additive `zgauss` Gaussian line component to the absorbed power-law model. We note that two objects out of our sample required fitting with an Fe K$\alpha$ line: Mrk 595 and RBS 1037. In addition, we test for the presence of spectral features due to reprocessing by adding a `pexrav` component (Magdziarz & Zdziarski 1995). We fixed elemental abundances to solar and kept the inclination angle fixed at the default value of 60°. We found that the reduced $\chi^2$ values and best-fit parameters from modeling with `pexrav` were similar to those from fitting an absorbed cutoff power-law for the majority of the sources in our sample, indicating that the addition of a reflection component does not significantly modify fit results and thus is not required by the data. Futhermore, we found that the null hypothesis probability exceeds 50 % for many of our sources when fitting with an absorbed cutoff power-law; we found the mean null hypothesis probability of our sample to be 43 %. We note that we chose a reflection model for one source (2MASX J19301380+3410495) due to best-fit parameters such as the photon index being more physically reasonable compared to the absorbed cutoff power-law model. We also note that the reduced $\chi^2$ for Mrk 9 is relatively high due to increased scatter in the data near $\sim 10$ keV and 30 keV, which do not correspond to any known physical features. We summarize some of the key best-fit spectral parameters for our sample in Table 3 of the appendix. We did not find any sources in our sample with significant line of sight absorption ($> 5 \times 10^{23}$ cm$^{-2}$), with most sources having hydrogen column densities constrained to be $< 10^{22}$ cm$^{-2}$. Figure 3 presents an example *NuSTAR* spectrum for a potential low-cutoff candidate in our sample, 2MASX J19301380+3410495, for which we measured $E_{\rm cut}$ to be $23^{+29}_{-9}$ keV.

## 3. RESULTS AND DISCUSSION

In this section, we present limits on the high-energy cutoff, $E_{\rm cut}$, found from spectral modeling of our sample. We then present the location of our sources on the $\theta - l$ plane for AGN coronae, and discuss the implications of sources with low values of $E_{\rm cut}$ on the heating and cooling mechanisms operating in the corona.

### 3.1. *Cutoff Constraints*

The distribution of lower limits on the high energy cutoff for our sample is presented in Figure 4. The histogram shows a number of AGN with lower limits on $E_{\rm cut}$ below 100 keV. Typical values of $E_{\rm cut}$ for AGN generally range from $\sim 100$ keV to 300 keV (Dadina 2007; Malizia et al. 2014; Ricci et al. 2017); we note Gilli et al. (2007) comment that the mean value of $E_{\rm cut}$ for AGN must not exceed several hundred keV, in order to avoid overproducing the cosmic X-ray background above 100 keV.
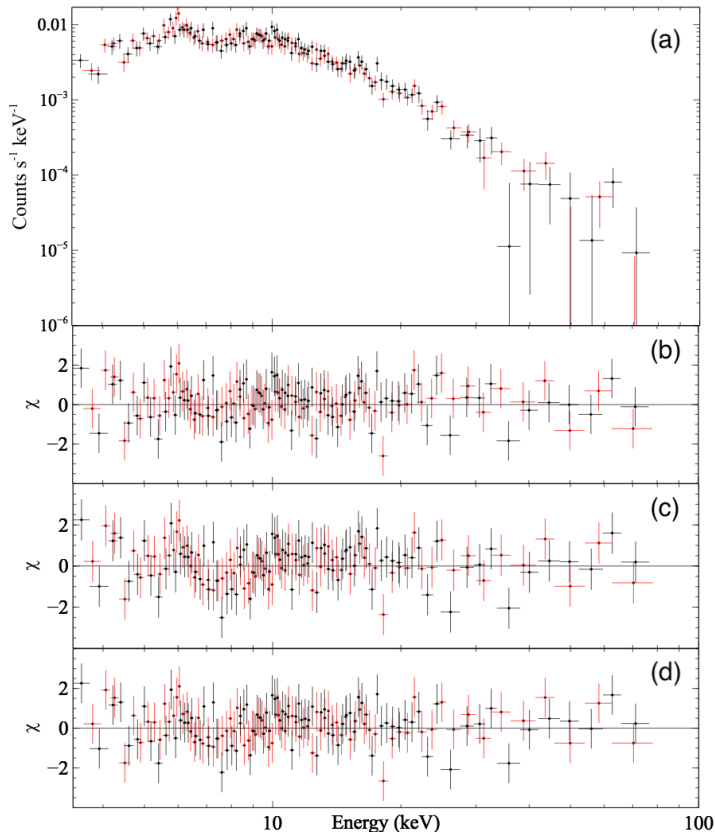
FIG. 3.— *NuSTAR* hard X-ray spectrum of a candidate low cut-off AGN 2MASX J19301380+3410495 (a), alongside fit residuals for (b) an absorbed power-law model ($\chi^2/\text{dof} = 155.1/161$) (c) absorbed power-law model with a high-energy cutoff ($\chi^2/\text{dof} = 144.4/160$) and (d) absorbed cutoff power-law with reflection modeled via `pexrav` ($\chi^2/\text{dof} = 138/160$). Black points correspond to FPMA data while points in red correspond to FPMB.
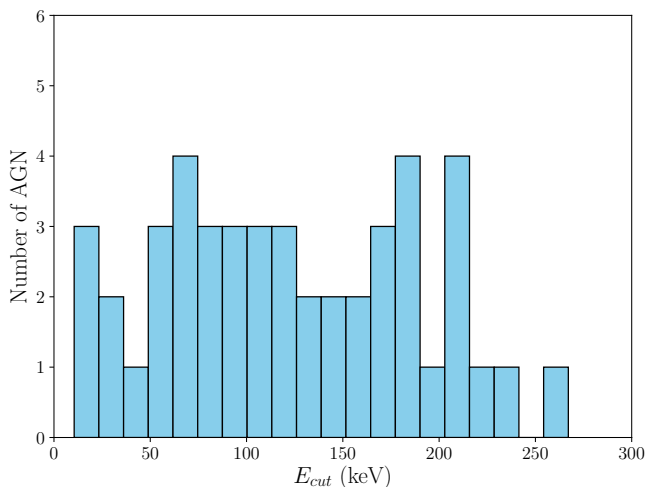


FIG. 4.— Distribution of lower limits on $E_{\text{cut}}$ for our Sy1 AGN sample from modeling *NuSTAR* data.

Despite the fact that the quality of *NuSTAR* data in the hard X-ray band exceeds any previous observations of
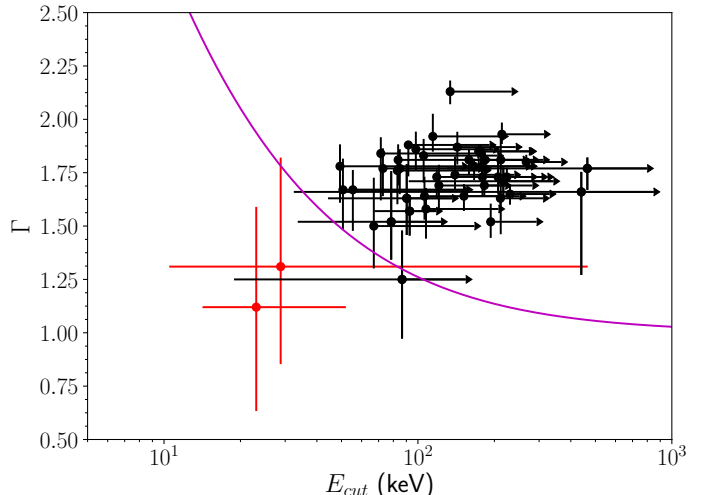


FIG. 5.— $E_{\text{cut}}$ vs photon index $\Gamma$ for our sample. Points in red denote candidate sources with low coronal high-energy cutoffs for which both upper and lower limits on $E_{\text{cut}}$ were measured. The purple line corresponds to theoretical constraints from Petrucci et al. (2001) for $\tau = 6$.

our targets, the cutoff power-law model does still display a degree of degeneracy in the derived photon index ($\Gamma$) and $E_{\text{cut}}$. In order to verify that our constraints on $E_{\text{cut}}$ are physically reasonable, in Figure 5 we compare our derived $\Gamma$ and $E_{\text{cut}}$ values to curves of constant optical depth in the $E_{\text{cut}}$–$\Gamma$ parameter space. The purple line in Figure 5 corresponds to theoretical constraints from Petrucci et al. (2001) for an optical depth $\tau = 6$. We use the relationship derived for a slab geometry of the corona by Petrucci et al. (2001) to calculate the optical depth as a function of $\Gamma$ and $E_{\text{cut}}$:

$$\Gamma = \sqrt{\frac{9}{4} + \frac{511 \text{ keV}}{\tau k T_e (1 + \tau/3)}} - \frac{1}{2}. \qquad (2)$$

AGN coronae are typically thought to be optically thin ($\tau < 1$) (Zdziarski 1985; Stern et al. 1995), though some have been constrained to $\tau \sim 3$ based on high-quality *NuSTAR* data (e.g., Baloković et al. 2015; Tortosa et al. 2017; Kara et al. 2017). Combinations of $\Gamma$ and $E_{\text{cut}}$ that correspond to $\tau > 6$ can be considered to result from a degeneracy between model parameters and therefore are unphysical. With this particular assumption we suspect that for 3 targets our results may be unrealistic; if, for example, $\tau < 10$ is chosen, then no targets fall in this category. However, sources lying near or below the line with $\tau = 6$ were not removed from our sample, as the limited *NuSTAR* data quality with a short, 20 ks exposure does not rule out physically reasonable values of the photon index.

We investigate the presence of model degeneracies in the sources with the lowest measured $E_{\text{cut}}$ constraints (2MASX J19301380+3410495 & 1RXS J034704.9-302409) by exploring the $E_{\text{cut}}$–$\Gamma$ parameter space in XSPEC. Figure 6 shows the contour plots of the photon index against the high-energy cutoff for these sources. Whilst there is some degree of degeneracy be-
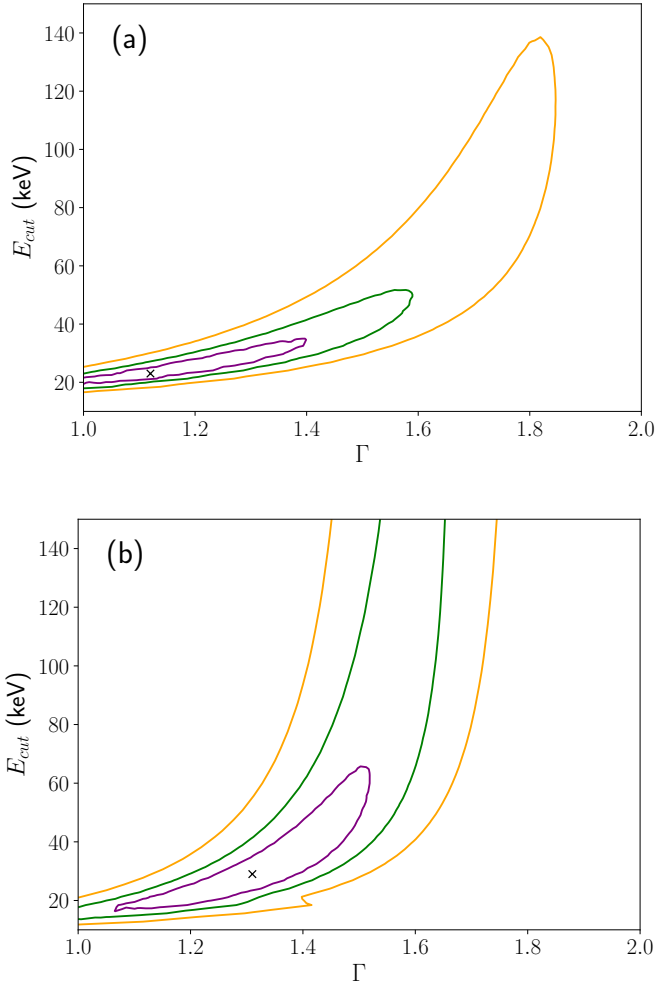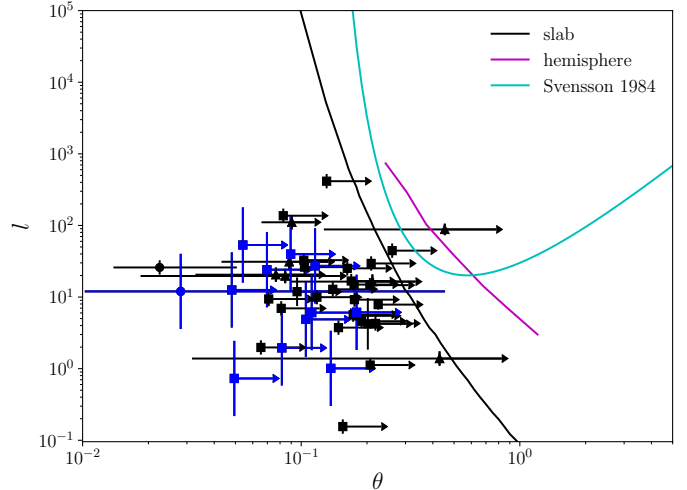
FIG. 7.— The $\theta - l$ plane for *NuSTAR*-observed Sy1 AGN. Solid lines correspond to pair lines for different coronal geometries. Circled points are candidate low cutoff sources for which both upper and lower limits on $E_{\rm cut}$ were measured. Triangles denote sources with a best-fit value and lower limit on $E_{\rm cut}$. Squares denote sources with only lower limits on $E_{\rm cut}$. Blue points indicate sources for which the black hole mass was taken to be the median black hole mass of the type 1 AGN in the BAT AGN Spectroscopic Survey (BASS) (Koss et al. 2017).



FIG. 6.— $E_{\rm cut}$–$\Gamma$ contour plots for *NuSTAR* observations of the candidate low cutoff Sy1s (a) 2MASX J19301380+3410495 (b) 1RXS J034704.9-302409. The solid purple, green and yellow contours correspond to the 68, 90 and 99 % confidence levels, respectively. The black cross represents the best fit values of the parameters from applying the relevant model given in Table 3.

tween these two parameters, the value of $E_{\rm cut}$ is constrained to low values over the range of physically reasonable photon index values at the 68 % confidence level.

### 3.2. *The $\theta - l$ Plane*

In constructing the observational $\theta - l$ plane, we convert from $E_{\rm cut}$ to the coronal temperature using $k_B T_e = E_{\rm cut}/2$ (Petrucci et al. 2001). In calculating $l$, we assume a conservative value of $10R_g$ for the coronal radius $R$, as adopted in Fabian et al. (2015), as the majority of the sources in our sample lack the required X-ray reflection modeling or reverberation measurements to place constraints on coronal size. We estimated the source luminosity $L$, from the flux in the 0.1–200 keV band, which was extrapolated from the applied spectral model. We convert the unabsorbed 0.1–200 keV flux obtained from spectral modeling to luminosity using luminosity distance values from NED. Black hole mass estimates, where available, were taken from Koss et al. (2017). The values of $M_{\rm BH}$ used in Koss et al. (2017) were obtained from a combination of broad Balmer emission line mea-

surements, direct techniques such as X-ray reverberation mapping, and the $M_{\rm BH} - \sigma_*$ relation of Kormendy & Ho (2013). We have black hole mass measurements obtained from the literature for 34 of the 46 sources in our sample. For sources with no published black hole mass, we use the median black hole mass of the Sy 1–1.5 AGN in the BAT AGN Spectroscopic Survey (BASS) (Koss et al. 2017), $\log(M_{\rm BH}/M_\odot) = 7.97 \pm 0.52$.

We note that the precise location of AGN on the $\theta - l$ plane is dependent on general relativistic effects, such as gravitational redshift and light bending. Processes such as light bending introduce inclination-dependent corrections to $l$. These corrections depend on the geometry of the corona, which is currently highly uncertain. Therefore, due to the large uncertainties associated with model-based relativistic corrections, we do not include general relativistic effects here.

Figure 7 presents the location of our sources on the $\theta - l$ plane, in addition to theoretical pair lines for different coronal geometries. Runaway pair production occurs to the right of the pair lines, as described in the introduction. Modeling the corona as an isolated electron cloud, Svensson (1984) estimated the pair production line to have the analytical form

$$l \sim 10\theta^{5/2} e^{1/\theta}. \qquad (3)$$

Stern et al. (1995) also computed the pair balance line for a slab and hemispherical corona respectively, located above a reflecting accretion disk. The solid black and purple lines in Figure 7 correspond to these geometries.

Our results show that most of the AGN coronae in our sample are clustered near the lines for runaway pair production, similar to the results found by Fabian et al. (2015) for *NuSTAR*-observed AGN and black hole binaries (BHB). The pair lines thus appear to correspond to a physical boundary, constraining sources to that region.

A few AGN are located away from the pair line boundary, hinting at low coronal temperatures. Note that we have assumed that the corona is homogeneous and at a single temperature, whereas in reality there may be a range of temperatures. This may result in a mean temperature at a lower value due to Compton cooling (Fabian et al. 2015).

Recent detections of low coronal cutoffs have been made within the *NuSTAR* band, such as Tortosa et al. (2017), Kara et al. (2017) and Xu et al. (2017). For example, Kara et al. (2017) measured $T_e = 15 \pm 2$ keV for the narrow-line Sy1 Ark 564, making it one of the lowest temperature coronae observed by *NuSTAR* to date. Multiple explanations have been proposed for the origin of low temperature coronae. In the case of an AGN accreting close to the Eddington limit, the stronger radiation field may enhance Compton cooling in comparison with sub-Eddington Seyferts (Kara et al. 2017). For sources accreting well below the Eddington limit, the relatively low coronal temperatures may be attributed to highly effective cooling in some AGN due to, e.g., high spin and the resulting higher seed photon temperature. Low temperatures may also arise from particularly weak coronal heating mechanisms, or more effective cooling due to multiple scatterings in a corona with high optical depth (e.g., Tortosa et al. 2017). Naively, when the optical depth in the corona exceeds unity, multiple inverse Compton scatterings transfer a proportionally higher fraction of the stored thermal energy to coronal luminosity. However, coronae are complex systems, and many coupled physical processes determine the electron temperature.

Another possibility is that the corona consists of a hybridized plasma, containing both thermal and non-thermal particles (e.g., Zdziarski et al. 1993; Ghisellini et al. 1993; Fabian et al. 2017). In such a system, the corona is highly magnetized and compact, and thus heating and cooling are so intense that electrons do not have time to thermalize before they are cooled by inverse Compton scattering. The presence of only a small fraction of non-thermal electrons with energies above 1 MeV can result in runaway pair production. The cooled electron-positron pairs may redistribute their available energy, thereby reducing the mean energy per particle and decreasing the coronal temperature. Such cooling would produce a hard non-thermal tail and an annihilation feature at 511 keV. Hard X-ray data of very high quality are necessary to distinguish between a hybrid, pair-dominated plasma and cooler, fully thermal plasma incapable of pair production.

## 4. FUTURE OBSERVATIONS

The $E_{\rm cut}$ constraints presented here are based on snapshot $\sim 20$ ks *NuSTAR* observations of a sample of bright Sy1 galaxies, and identified several sources which potentially have high-energy cutoffs within the *NuSTAR* band (i.e., 3–79 keV). Future work will involve performing longer exposure *NuSTAR* observations of AGN from our sample that display hints of a low coronal cutoff, which will aid in removing model degeneracies and more tightly constrain $E_{\rm cut}$, in order to determine the coronal temperature. In choosing AGN from our sample for longer exposure *NuSTAR* observations, we performed 5000 simulations of the spectra of candidate low $E_{\rm cut}$ AGN from our sample in XSPEC, for exposure times of 50 ks and
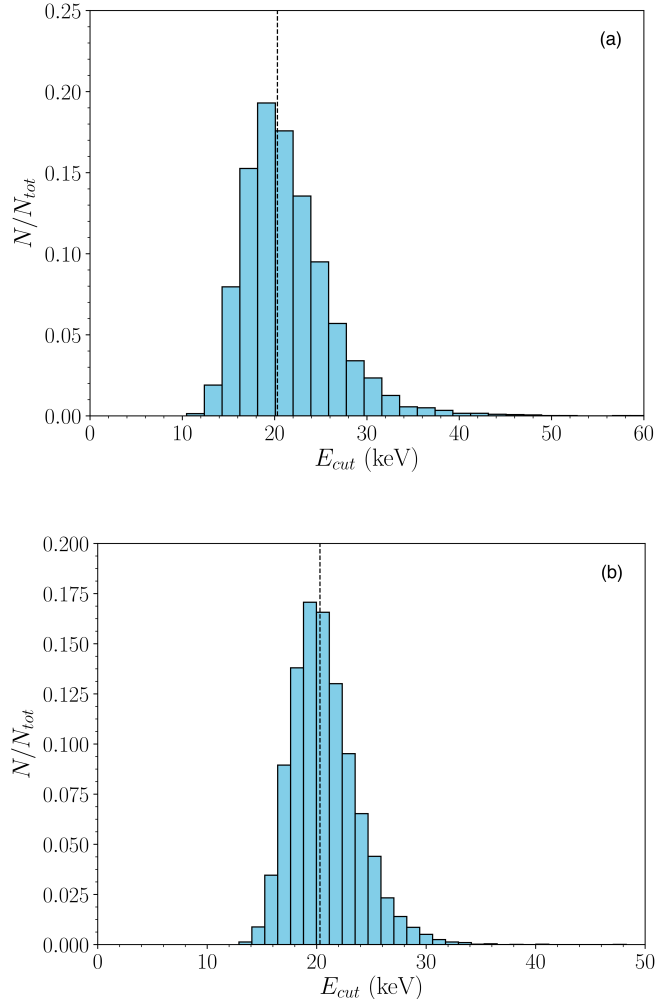


Fig. 8.— Distributions of $E_{\rm cut}$ values for 5000 simulations of the *NuSTAR* spectrum of a candidate low cutoff AGN, 2MASX J19301380+3410495. Dotted lines denote the input $E_{\rm cut}$ value assumed for simulated spectra. Simulations were performed for exposure times of (a) 50 ks and (b) 100 ks.

100 ks. From the simulated spectra, we plotted distributions of the best-fit value of $E_{\rm cut}$ found from applying an absorbed cutoff power-law model, in addition to lower limits and upper limits on $E_{\rm cut}$. The plots in Figure 8 show distributions of values of $E_{\rm cut}$ for one such candidate low cutoff source, 2MASX J19301380+3410495. Table 1 summarizes the mean values of $E_{\rm cut}$ and its lower and upper limits obtained from our simulations for some candidate low cutoff AGN in our sample.

The simulation results show that the distributions peak at low values of $E_{\rm cut}$, and at similar values for both a 50 ks and 100 ks exposure. We conclude from our results that a 50 ks exposure should be sufficient to constrain the high-energy cutoff in our sample of candidate low cutoff AGN.

## 5. SUMMARY

In this work, we have investigated the coronal properties of a sample of *Swift*/BAT selected Seyfert 1 AGN that have been observed with *NuSTAR*. We individually modeled the *NuSTAR* spectra of all sources in our

TABLE 1
Mean values of the high-energy cutoff, its lower and upper limits from simulated *NuSTAR* spectra, for
*Swift*/BAT-selected Sy1 AGN

| Name | Exposure Time | $E_{cut}$ | $E_{cut}$ lower limit | $E_{cut}$ upper limit |
|---|---|---|---|---|
| | (ks) | (keV) | (keV) | (keV) |
| 1RXS J034704.9-302409 | 50 | 92.7 | 17.1 | 118.8 |
| | 100 | 54.6 | 19.2 | 111.8 |
| 2MASX J19301380+3410495 | 50 | 21.4 | 15.7 | 33.0 |
| | 100 | 20.7 | 16.7 | 27.0 |
| Mrk 1393 | 50 | 189.0 | 43.5 | 191.7 |
| | 100 | 155.0 | 45.0 | 199.7 |
| SDSS J104326d47+110524.2 | 50 | 170.4 | 46.3 | 203.2 |
| | 100 | 134.1 | 52.1 | 206.5 |
| UGC 06728 | 50 | 162.6 | 59.4 | 234.8 |
| | 100 | 127.5 | 67.6 | 222.8 |

sample and searched for sources with hints of low coronal cutoffs, observable within the *NuSTAR* band. We mapped out the location of the sources in our sample on the compactness-temperature diagram for AGN coronae, and found that the majority of sources lie near the boundary for runaway pair production. The pair production line corresponds to a physical boundary, constraining AGN to that region. A few AGN located away from the pair lines may possess low coronal temperatures; deeper 50 ks *NuSTAR* observations will be performed of these sources to constrain the coronal temperature and optical depth. The detection of low coronal cutoffs may be explained via scenarios such as a strong radiation field, large optical depth, or a hybrid pair-dominated plasma. Further computations with hybrid plasma models, taking into account general relativistic effects, will help elucidate in more detail the heating and cooling mechanisms operating in the corona.

We would like to thank the referee for their help-

REFERENCES

Arnaud, K. 1996, in ASP Conf. Series, Vol. 101, Astronomical Data Analysis Software and Systems, ed. G. H. Jacoby & J. Barnes, 17
Ballantyne, D. R., Bollenbacher, J. M., Brenneman, L. W., et al. 2014, ApJ, 794, 62
Baloković, M., Matt, G., Harrison, F. A., et al. 2015, ApJ, 800, 62
Baumgartner, W. H., Tueller, J., Markwardt, C. B., et al. 2013, ApjS, 207, 19
Brenneman, L. W., Madejski, G., Fuerst, F., et al. 2014, ApJ, 781, 83
Dadina, M. 2007, A&A, 461, 1209
Emmanoulopoulos, D., Papadakis, I. E., Dovčiak, M., & McHardy, I. M. 2014, MNRAS, 439, 3931
Fabian, A. C., Lohfink, A., Belmont, R., Malzac, J., & Coppi, P. 2017, MNRAS, 467, 2566
Fabian, A. C., Lohfink, A., Kara, E., et al. 2015, MNRAS, 451, 4375
Fabian, A. C., Zoghbi, A., Ross, R. R., et al. 2009, Nature, 459, 540
Gehrels, N., Chincarini, G., Giommi, P., et al. 2004, ApJ, 611, 1005
Ghisellini, G., Haardt, F., & Fabian, A. C. 1993, MNRAS, 263

Gilli, R., Comastri, A., & Hasinger, G. 2007, A&A, 463, 79
Guilbert, P. W., Fabian, A. C., & Rees, M. J. 1983, MNRAS, 205, 593
Haardt, F., & Maraschi, L. 1993, ApJ, 413, 507
Harrison, F. A., Craig, W. W., Christensen, F. E., et al. 2013, ApJ, 770, 103
Kalberla, P. M. W., Burton, W. B., Hartmann, D., et al. 2005, A&A, 440, 775
Kara, E., Fabian, A. C., Cackett, E. M., Miniutti, G., & Uttley, P. 2013, MNRAS, 430, 1408
Kara, E., García, J. A., Lohfink, A., et al. 2017, MNRAS, 468, 3489
Kormendy, J., & Ho, L. C. 2013, ARA&A, 51, 511
Koss, M., Trakhtenbrot, B., Ricci, C., et al. 2017, ApJ, 850, 74
Madsen, K. K., Harrison, F. A., Markwardt, C. B., et al. 2015, ApJ, 220, 8
Magdziarz, P., & Zdziarski, A. A. 1995, MNRAS, 273, 837
Malizia, A., Molina, M., Bassani, L., et al. 2014, ApJL, 782, L25
Marinucci, A., Matt, G., Miniutti, G., et al. 2014, ApJ, 787, 83
Massaro, E., Giommi, P., Leto, C., et al. 2009, A&A, 495, 691
Perri, M., Puccetti, S., Spagnuolo, N., et al. 2014, The NuSTAR Data Analysis Software Guide v1.7

Petrucci, P. O., Haardt, F., Maraschi, L., et al. 2001, ApJ, 556, 716

Ricci, C., Trakhtenbrot, B., Koss, M. J., et al. 2017, ApJS, 233, 17

Rybicki, G. B., & Lightman, A. P. 1979, Radiative processes in astrophysics (Wiley-Interscience, New York)

Stern, B. E., Poutanen, J., Svensson, R., Sikora, M., & Begelman, M. C. 1995, ApJL, 449, L13

Svensson, R. 1982, ApJ, 258, 335

—. 1984, MNRAS, 209, 175

Tortosa, A., Marinucci, A., Matt, G., et al. 2017, MNRAS, 466, 4193

Verner, D. A., Ferland, G. J., Korista, K. T., & Yakovlev, D. G. 1996, ApJ, 465, 487

Wilms, J., Allen, A., & McCray, R. 2000, ApJ, 542, 914

Xu, Y., Baloković, M., Walton, D. J., et al. 2017, ApJ, 837, 21

Zdziarski, A. A. 1985, ApJ, 289, 514

Zdziarski, A. A., Poutanen, J., & Johnson, W. N. 2000, ApJ, 542, 703

Zdziarski, A. A., Zycki, P. T., & Krolik, J. H. 1993, ApJ, 414, L81

APPENDIX

TABLE 2
*NuSTAR* Observation Details for *Swift*/BAT–selected Sy1 AGN

| Name | Swift/BAT ID | Observation ID | Observation Date | Exposure Time (ks) | Total Counts |
|---|---|---|---|---|---|
| 1RXS J034704.9-302409 | SWIFT J0347.0-3027 | 60061039002 | 2013-03-15 | 6.4 | 13.5 |
| | | 60061039004 | 2013-03-24 | 12.7 | 20.4 |
| | | 60061039006 | 2013-04-02 | 9.5 | 21.9 |
| 1RXS J174538.1+290823 | SWIFT J1745.4+2906 | 60160674002 | 2014-12-09 | 20.3 | 2233 |
| 1RXS J213445.2-272551 | SWIFT J2134.9−2729 | 60061306002 | 2013-10-22 | 19.8 | 2178 |
| 2MASS J19334715+3254259 | SWIFT J1933.9+3258 | 60160714002 | 2016-05-31 | 12.6 | 3024 |
| 2MASX J04372814-4711298 | SWIFT J0437.4−4713 | 60160197002 | 2015-12-09 | 20.0 | 1500 |
| 2MASX J12313717-4758019 | SWIFT J1232.0−4802 | 60160498002 | 2016-08-21 | 19.3 | 1718 |
| 2MASX J15144217-8123377 | SWIFT J1513.8−8125 | 60061263002 | 2013-08-06 | 13.3 | 1011 |
| 2MASX J15295830-1300397 | SWIFT J1530.0−1300 | 60160617002 | 2017-02-14 | 24.2 | 2130 |
| 2MASX J19301380+3410495 | SWIFT J1930.5+3414 | 60160713002 | 2016-07-19 | 20.5 | 1701 |
| 2MASX J19380437-5109497 | SWIFT J1938.1−5108 | 60160716002 | 2016-07-15 | 21.8 | 2834 |
| 2MASX J20005575-1810274 | SWIFT J2001.0−1811 | 60061295002 | 2016-10-25 | 21.9 | 1367 |
| 2MASXi J1802473-145454 | SWIFT J1802.8−1455 | 60160680002 | 2016-05-01 | 20.0 | 6800 |
| 3C 227 | SWIFT J0947.7+0726 | 60061329002 | 2014-02-20 | 17.2 | 293 |
| | | 60061329004 | 2014-02-26 | 12.1 | 188 |
| 4C +18.51 | SWIFT J1742.2+1833 | 60160672002 | 2017-03-27 | 22.5 | 1080 |
| ESO 438-G009 | SWIFT J1110.6−2832 | 60160423002 | 2015-02-01 | 21.7 | 1302 |
| Fairall 1146 | SWIFT J0838.4−3557 | 60061082002 | 2014-07-27 | 21.3 | 4473 |
| Fairall 1203 | SWIFT J0001.6−7701 | 60160002002 | 2015-04-11 | 34.1 | 1739 |
| [HB89] 0241+622 | SWIFT J0244.8+6227 | 60160125002 | 2016-07-31 | 23.4 | 9126 |
| IGR J14471-6414 | SWIFT J1446.7−6416 | 60061257002 | 2013-05-28 | 15.0 | 975 |
| IGR J14552-5133 | SWIFT J1454.9−5133 | 60061259002 | 2013-09-19 | 21.9 | 2190 |
| IRAS 04392-2713 | SWIFT J0441.2−2704 | 60160201002 | 2015-12-20 | 19.5 | 2145 |
| LCRSB 232242.2-384320 | SWIFT J2325.5−3827 | 60160826002 | 2016-07-08 | 22.5 | 495 |
| Mrk 9 | SWIFT J0736.9+5846 | 60061326002 | 2013-10-29 | 23.3 | 1142 |
| Mrk 376 | SWIFT J0714.3+4541 | 60160288002 | 2015-04-07 | 24.2 | 1791 |
| Mrk 595 | SWIFT J0241.6+0711 | 60160119002 | 2017-01-18 | 21.3 | 873 |
| Mrk 732 | SWIFT J1113.6+0936 | 60061208002 | 2013-06-11 | 26.3 | 3419 |
| Mrk 739E | SWIFT J1136.0+2132 | 60260008002 | 2017-03-16 | 18.5 | 1277 |
| Mrk 813 | SWIFT J1427.5+1949 | 60160583002 | 2017-01-23 | 24.6 | 2952 |
| Mrk 817 | SWIFT J1436.4+5846 | 60160590002 | 2015-07-25 | 21.9 | 2847 |
| Mrk 841 | SWIFT J1504.2+1025 | 60101023002 | 2015-07-14 | 23.4 | 6084 |
| Mrk 1018 | SWIFT J0206.2−0019 | 60160087002 | 2016-02-10 | 21.6 | 583 |
| Mrk 1044 | SWIFT J0230.2−0900 | 60160109002 | 2016-02-08 | 21.7 | 2821 |
| Mrk 1310 | SWIFT J1201.2−0341 | 60160465002 | 2016-06-17 | 21.1 | 2743 |
| Mrk 1393 | SWIFT J1508.8−0013 | 60160607002 | 2016-01-19 | 22.4 | 896 |
| NGC 0985 | SWIFT J0234.6−0848 | 60061025002 | 2013-08-11 | 13.9 | 2363 |
| PG 0804+761 | SWIFT J0810.9+7602 | 60160322002 | 2016-04-02 | 17.3 | 1903 |
| PKS 0558-504 | SWIFT J0559.8−5028 | 60160254002 | 2016-11-19 | 21.0 | 2940 |
| RBS 0295 | SWIFT J0214.9−6432 | 60061021002 | 2017-01-14 | 23.3 | 1887 |
| RBS 0770 | SWIFT J0923.7+2255 | 60061092002 | 2012-12-26 | 18.9 | 6426 |
| RBS 1037 | SWIFT J1149.3−0414 | 60061215002 | 2017-02-02 | 40.7 | 2198 |
| RBS 1125 | SWIFT J1232.1+2009 | 60061229002 | 2016-07-28 | 20.0 | 1280 |
| SBS 1136+594 | SWIFT J1139.1+5913 | 60160443002 | 2014-12-26 | 23.5 | 3760 |
| SDSS J104326.47+110524.2 | SWIFT J1043.4+1105 | 60160406002 | 2016-06-14 | 20.1 | 137 |
| UGC 06728 | SWIFT J1143.7+7942 | 60160450002 | 2016-07-10 | 22.6 | 2486 |
| UM 614 | SWIFT J1349.7+0209 | 60160560002 | 2015-03-31 | 18.2 | 2002 |
| WKK 1263 | SWIFT J1241.6−5748 | 60160510002 | 2016-04-27 | 16.4 | 7872 |

TABLE 3
Redshifts, black hole masses and best-fit spectral parameters from fitting *NuSTAR* data for our *Swift*/BAT-selected Sy1 AGN sample

| Source | Redshift | $\log(M_{\mathrm{BH}}/M_\odot)^A$ | $\Gamma$ | $E_{\mathrm{cut}}$ (keV) | $F^B_{0.1-200}$ $10^{-12}$ erg cm$^{-2}$ s$^{-1}$ | $\chi^2$/dof | Model$^C$ |
|---|---|---|---|---|---|---|---|
| 1RXS J034704.9-302409* | 0.095 | 7.97±0.52 | $1.31^{+0.51}_{-0.46}$ | $29^{+437}_{-18}$ | $1.12^{+0.38}_{-0.10}$ | 50.9/50 | 1 |
| 1RXS J174538.1+290823 | 0.111 | 8.82±0.10 | $1.76^{+0.06}_{-0.16}$ | $\geq 83$ | $8.59^{+0.91}_{-0.89}$ | 181.5/187 | 1 |
| 1RXS J213445.2-272551 | 0.067 | 6.99±0.10 | $1.77^{+0.09}_{-0.12}$ | $\geq 85$ | $7.62^{+0.73}_{-0.38}$ | 155.8/175 | 1 |
| 2MASS J19334715+3254259 | 0.057 | 7.88±0.10 | $1.78^{+0.04}_{-0.06}$ | $\geq 166$ | $15.3^{+0.6}_{-0.6}$ | 236.3/225 | 1 |
| 2MASX J04372814-4711298* | 0.053 | 7.97±0.52 | $1.92^{+0.11}_{-0.07}$ | $\geq 114$ | $5.08^{+0.56}_{-0.25}$ | 147.5/123 | 1 |
| 2MASX J12313717-4758019* | 0.028 | 7.97±0.52 | $1.81^{+0.07}_{-0.12}$ | $\geq 84$ | $5.88^{+0.75}_{-0.46}$ | 107.8/139 | 1 |
| 2MASX J15144217-8123377 | 0.068 | 8.96±0.10 | $1.66^{+0.09}_{-0.39}$ | $\geq 32$ | $6.67^{+0.94}_{-1.24}$ | 95.3/86 | 1 |
| 2MASX J15295830-1300397* | 0.104 | 7.97±0.52 | $1.73^{+0.04}_{-0.10}$ | $\geq 119$ | $5.49^{+0.25}_{-0.25}$ | 172.4/170 | 1 |
| 2MASX J19301380+3410495 | 0.063 | 8.15±0.10 | $1.12^{+0.47}_{-0.49}$ | $23^{+29}_{-9}$ | $22.9^{+5.98}_{-3.77}$ | 138/160 | 2 |
| 2MASX J19380437-5109497 | 0.040 | 7.23±0.10 | $1.83^{+0.08}_{-0.12}$ | $\geq 105$ | $9.03^{+0.78}_{-0.65}$ | 214.2/215 | 1 |
| 2MASX J20005575-1810274 | 0.037 | 8.07±0.36 | $1.73^{+0.08}_{-0.08}$ | $\geq 207$ | $9.62^{+0.79}_{-0.76}$ | 285.1/250 | 1 |
| 2MASXi J1802473-145454 | 0.003 | 7.76±0.10 | $1.81^{+0.05}_{-0.07}$ | $\geq 159$ | $23.9^{+1.3}_{-1.2}$ | 466.3/451 | 1 |
| 3C 227 | 0.086 | 8.61±0.10 | $1.63^{+0.16}_{-0.17}$ | $\geq 44$ | $11.7^{+1.1}_{-0.9}$ | 331/347 | 1 |
| 4C +18.51* | 0.186 | 7.97±0.52 | $1.67^{+0.09}_{-0.19}$ | $\geq 55$ | $3.04^{+0.34}_{-0.20}$ | 73.2/100 | 1 |
| ESO 438-G009* | 0.024 | 7.97±0.52 | $1.74^{+0.09}_{-0.07}$ | $\geq 140$ | $3.95^{+0.23}_{-0.23}$ | 92.3/113 | 1 |
| Fairall 1146* | 0.031 | 7.97±0.52 | $1.81^{+0.04}_{-0.05}$ | $\geq 184$ | $14.1^{+0.9}_{-0.5}$ | 365.9/326 | 1 |
| Fairall 1203* | 0.058 | 7.97±0.52 | $1.58^{+0.11}_{-0.07}$ | $\geq 108$ | $3.37^{+0.38}_{-0.33}$ | 139.4/150 | 1 |
| [HB89] 0241+622 | 0.044 | 8.09±0.10 | $1.63^{+0.04}_{-0.05}$ | $\geq 211$ | $24.1^{+1.0}_{-7.4}$ | 631.1/565 | 1 |
| IGR J14471-6414 | 0.053 | 7.70±0.10 | $1.77^{+0.09}_{-0.13}$ | $\geq 73$ | $4.08^{+0.51}_{-0.28}$ | 84.3/82 | 1 |
| IGR J14552-5133 | 0.016 | 6.86±0.10 | $1.73^{+0.03}_{-0.09}$ | $\geq 180$ | $6.43^{+0.35}_{-0.25}$ | 191.9/181 | 1 |
| IRAS 04392-2713* | 0.084 | 7.97±0.52 | $1.84^{+0.08}_{-0.22}$ | $\geq 71$ | $7.82^{+0.71}_{-0.44}$ | 200.8/173 | 1 |
| LCRSB 232242.2-384320* | 0.036 | 7.97±0.52 | $1.67^{+0.14}_{-0.19}$ | $\geq 51$ | $1.44^{+0.20}_{-0.13}$ | 50.9/46 | 1 |
| Mrk 9 | 0.040 | 7.59±0.10 | $1.52^{+0.08}_{-0.08}$ | $\geq 193$ | $2.83^{+0.19}_{-0.18}$ | 155.1/100 | 1 |
| Mrk 376 | 0.056 | 8.17±0.10 | $1.64^{+0.06}_{-0.07}$ | $\geq 152$ | $4.38^{+0.37}_{-0.20}$ | 170.3/147 | 1 |
| Mrk 595 | 0.027 | 8.28±0.10 | $1.50^{+0.23}_{-0.20}$ | $\geq 67$ | $2.62^{+0.43}_{-0.33}$ | 79.5/76 | 3 |
| Mrk 732 | 0.029 | 7.23±0.10 | $1.85^{+0.07}_{-0.07}$ | $\geq 173$ | $7.95^{+0.31}_{-0.31}$ | 269.6/258 | 1 |
| Mrk 739E | 0.030 | 7.14±0.10 | $1.87^{+0.07}_{-0.08}$ | $\geq 143$ | $4.80^{+0.30}_{-0.29}$ | 113.1/106 | 1 |
| Mrk 813 | 0.110 | 8.87±0.10 | $1.85^{+0.03}_{-0.10}$ | $\geq 177$ | $7.95^{+0.31}_{-0.31}$ | 269.6/230 | 1 |
| Mrk 817 | 0.031 | 7.59±0.07 | $1.65^{+0.04}_{-0.05}$ | $\geq 230$ | $7.82^{+0.36}_{-0.30}$ | 263.1/214 | 1 |
| Mrk 841 | 0.036 | 7.81±0.10 | $1.78^{+0.05}_{-0.06}$ | $\geq 179$ | $17.9^{+1.0}_{-0.7}$ | 403.9/425 | 1 |
| Mrk 1018 | 0.042 | 8.03±0.10 | $1.81^{+0.14}_{-0.35}$ | $\geq 212$ | $1.76^{+0.46}_{-0.24}$ | 50.5/51 | 1 |
| Mrk 1044 | 0.016 | 6.44±0.10 | $1.93^{+0.05}_{-0.05}$ | $\geq 214$ | $8.74^{+0.36}_{-0.36}$ | 215.2/205 | 1 |
| Mrk 1310 | 0.019 | 6.21±0.08 | $1.77^{+0.05}_{-0.10}$ | $\geq 130$ | $8.68^{+0.72}_{-0.32}$ | 215/217 | 1 |
| Mrk 1393 | 0.054 | 7.87±0.10 | $1.25^{+0.23}_{-0.28}$ | $\geq 19$ | $2.07^{+0.47}_{-0.21}$ | 109.8/79 | 1 |
| NGC 0985 | 0.043 | 7.92±0.10 | $1.69^{+0.10}_{-0.11}$ | $\geq 121$ | $11.7^{+1.1}_{-0.97}$ | 187/195 | 1 |
| PG 0804+761 | 0.100 | 8.73±0.05 | $1.69^{+0.07}_{-0.05}$ | $\geq 183$ | $6.85^{+0.34}_{-0.33}$ | 126.3/155 | 1 |
| PKS 0558-504 | 0.137 | 7.33±0.10 | $2.13^{+0.05}_{-0.06}$ | $\geq 134$ | $10.4^{+3.7}_{-0.39}$ | 217.9/206 | 1 |
| RBS 0295* | 0.074 | 7.97±0.52 | $1.78^{+0.10}_{-0.17}$ | $\geq 49$ | $5.32^{+0.51}_{-0.42}$ | 149.3/153 | 1 |
| RBS 0770 | 0.032 | 7.34±0.10 | $1.80^{+0.03}_{-0.03}$ | $\geq 267$ | $22.8^{+0.59}_{-0.58}$ | 400.3/434 | 1 |
| RBS 1037* | 0.084 | 7.97±0.52 | $1.88^{+0.01}_{-0.15}$ | $\geq 92$ | $3.77^{+0.17}_{-0.19}$ | 180.6/185 | 3 |
| RBS 1125 | 0.063 | 7.76±0.20 | $1.86^{+0.08}_{-0.10}$ | $\geq 98$ | $4.11^{+0.25}_{-0.25}$ | 109.1/107 | 1 |
| SBS 1136+594 | 0.060 | 7.98±0.10 | $1.71^{+0.06}_{-0.08}$ | $\geq 92$ | $10.6^{+0.4}_{-0.4}$ | 295/285 | 1 |
| SDSS J104326.47+110524.2 | 0.048 | 7.91±0.10 | $1.52^{+0.24}_{-0.18}$ | $\geq 34$ | $4.13^{+0.69}_{-0.23}$ | 122/122 | 1 |
| UGC 06728 | 0.006 | 5.66±0.10 | $1.57^{+0.07}_{-0.11}$ | $\geq 67$ | $6.96^{+0.30}_{-0.30}$ | 227.3/208 | 1 |
| UM 614 | 0.033 | 7.09±0.10 | $1.64^{+0.09}_{-0.11}$ | $\geq 106$ | $7.31^{+0.71}_{-0.50}$ | 162.7/172 | 1 |
| WKK 1263 | 0.024 | 8.25±0.10 | $1.73^{+0.04}_{-0.04}$ | $\geq 224$ | $31.6^{+1.5}_{-1.1}$ | 470.3/503 | 1 |

Note. — Sources marked with an asterisk (*) correspond to AGN whose black hole masses were taken to be the median black hole mass of the type 1 AGN in the BAT AGN Spectroscopic Survey (BASS) (Koss et al. 2017).
$^A$ Reference: Koss et al. (2017).
$^B$ Unabsorbed 0.1 - 200 keV flux extrapolated from applied spectral model
$^C$ Applied XSPEC models: (1) `constant` $\times$ `TBabs` $\times$ `zwabs` $\times$ `cutoffpl`
(2) `constant` $\times$ `TBabs` $\times$ `zwabs` $\times$ `(cutoffpl + pexrav)`
(3) `constant` $\times$ `TBabs` $\times$ `zwabs` $\times$ `(cutoffpl + zgauss)`